

THE MASS RELATIONS BETWEEN SUPERMASSIVE BLACK HOLES AND THEIR HOST GALAXIES AT $1 < Z < 2$ WITH *HST*-WFC3

XUHEN DING^{1,2}, JOHN SILVERMAN³, TOMMASO TREU¹, ANDREAS SCHULZE⁶, MALTE SCHRAMM⁶, SIMON BIRRER¹, KNUD JAHNKE, FEDERICA DURAS^{4,5}, ANGELA BONGIORNO⁵, ET AL.

Draft version March 24, 2019

ABSTRACT

The tight correlations between the mass of a supermassive black hole (\mathcal{M}_{BH}) and its host galaxy properties suggests an evolutionary connection. A powerful way to test this co-evolution hypothesis is to trace the correlations back in cosmic time. For this purpose, we obtained multi-band *Hubble Space Telescope* of a sample of 32 X-ray-selected broad-line (type-1) AGN at $1.2 < z < 1.7$ (look-back time 8-10 Gyrs). By applying state-of-the-art tools to the images we obtained accurate host galaxy luminosity and stellar mass. The black hole mass (\mathcal{M}_{BH}) is based on published near-infrared spectroscopic observations of the broad $H\alpha$ and $H\beta$ emission lines, which avoids potential unknown systematic uncertainties associated with the less well calibrated UV lines C_{IV} or Mg_{II}, commonly used at these redshifts. We compare the $\mathcal{M}_{\text{BH}}-L_{\text{host}}$ and $\mathcal{M}_{\text{BH}}-M_*$ relations to those of local active galaxies, accounting for selection effects, to infer their evolution. The $\mathcal{M}_{\text{BH}}-L_{\text{host}}$ relation is inconsistent with the local one, accounting for passive evolution, indicating that at fixed mass BHs 8-10 Gyrs ago reside in less luminous galaxies than today. Furthermore, the $\mathcal{M}_{\text{BH}}-M_*$ of our high redshift sample is consistent with the local $\mathcal{M}_{\text{BH}}-M_{*\text{bulge}}$ relations. Considering that our sample are composed of bulge and disk components, the evolution of both correlations is consistent with a scenario where the black hole grows first, followed by morphological transformations of host galaxies from late to early-types.

Subject headings: galaxies: active — galaxies: evolution

1. INTRODUCTION

Most galactic nuclei are thought to harbor a supermassive black hole (BH), whose mass (\mathcal{M}_{BH}) is known to be correlated with the host properties, such as \mathcal{M}_{BH} -host luminosity (L_{host}), \mathcal{M}_{BH} -stellar mass (M_*) and \mathcal{M}_{BH} -stellar velocity dispersion (σ_*). These tight correlations indicate a connection between nuclear activity and galaxy formation and evolution (e.g., Magorrian et al. 1998; Ferrarese & Merritt 2000; Marconi & Hunt 2003; Gültekin et al. 2009; Beifiori et al. 2012; Häring & Rix 2004; Gebhardt et al. 2001; Graham et al. 2011). Currently, the physical mechanism that can produce such a tight relationship is unknown, due to the daunting range of scales between the BHs dynamical sphere and their host galaxy. On the one hand, cosmological simulations of structure formation are able to reproduce the mean local correlations considering the active galactic nucleus (AGN) feedback as the physical driver (Springel et al. 2005; Hopkins et al. 2008; Di Matteo et al. 2008; DeGraf et al. 2015). On the other hand, Peng (2007); Jahnke & Macciò (2011); Hirschmann et al. (2010) show that, without the need of physical coupling, another possibility is a statistical convergence from the galaxy mergers which reproduces the observed correlations.

A powerful way to understand the origin of these correla-

tions is to study them as a function of redshift, determining how and when they emerged and evolved over cosmic time (e.g., Treu et al. 2004; Salvander et al. 2006; Woo et al. 2006; Jahnke et al. 2009; Schramm & Silverman 2013). During the past decade, there has been much progress on this front at $z < 1$ using type 1 AGNs. For example, the work by Park et al. (2015); Treu et al. (2007a); Peng et al. (2006) demonstrated that \mathcal{M}_{BH} at fixed mass resided in less luminous galaxies than today. This offset can be explained by a scenario in which supermassive BHs were built up first with galaxy then growing around their deep potential wells. Similarly, the works by Bennert et al. (2011b); Woo et al. (2008) supported this general scenario from the observation of the $\mathcal{M}_{\text{BH}}-M_*$ and $\mathcal{M}_{\text{BH}}-\sigma_*$ relations. It should be kept in mind, however, that the evolution is detected at low significance given the considerable error bars, and some studies report results consistent with no evolution given their larger error bars Schramm & Silverman (2013); Sun et al. (2015); Cisternas et al. (2011).

In order to make progress it is important to reduced as much as possible the uncertainties and take great care of selection effects and systematic errors. First, one needs to deal with the inherent uncertainties in BH mass estimates using the so-called “virial” method. In particular, many studies rely on \mathcal{M}_{BH} estimates using the C_{IV} (or Mg_{II}) line that may have unknown systematics, such as non gravitational component of the BLR gas dynamics, when compared to local samples with masses based on broad Balmer lines (i.e. $H\alpha$ and $H\beta$, Schulze et al. 2018; Baskin & Laor 2005; Trakhtenbrot & Netzer 2012). Second, since the host information is swamped by the bright nuclear light, measuring the host galaxy properties is challenging. Great care is required for modeling the point spread function and whenever possible it is beneficial to study lensed quasars, since lensing magnifies the host image to lensed arcs (Peng et al. 2006; Ding et al. 2017a,b). Last

dxh@astro.ucla.edu

¹ Department of Physics and Astronomy, University of California, Los Angeles, CA, 90095-1547, USA

² School of Physics and Technology, Wuhan University, Wuhan 430072, China

³ Kavli Institute for the Physics and Mathematics of the Universe, The University of Tokyo, Kashiwa, Japan 277-8583 (Kavli IPMU, WPI)

⁴ Dipartimento di Matematica e Fisica, Universit Roma Tre, via della Vasca Navale 84, I-00146, Roma, Italy

⁵ INAF Osservatorio Astronomico di Roma, via Frascati 33, 00040 Monteporzio Catone, Italy

⁶ National Astronomical Observatory of Japan, Mitaka, Tokyo 181-8588, Japan

but not least, the selection function needs to be taken into account when interpreting the observations (Treu et al. 2007b; Lauer et al. 2007). For instance, it has been demonstrated (Schulze & Wisotzki 2011, 2014) that selecting bright AGNs at high redshift results in display steeper slopes than random ones, suggesting the selecting effects can exhibit faster evolution than a random sample. It is also important to consider the selection function when comparing the observed scaling relations with simulated ones (DeGraf et al. 2015).

In this study, we aim to make progress by making use of a large sample with high-quality data both for the measurement of both the host properties and the \mathcal{M}_{BH} , extending to the highest redshifts where evolutionary effects should be strongest (DeGraf et al. 2015). In practice, we aim to determine whether AGNs have begun to couple to their host galaxy at $1.2 < z < 1.7$, an epoch when supermassive BH close to its peak accretion history (Aird et al. 2015). In this redshift range, we measure 32 host galaxies properties using *HST* imaging data, and estimate their \mathcal{M}_{BH} based on the robust $H\alpha$ and $H\beta$, using the multi-object spectrograph Subaru/FMOS. Our study overcomes the limitations of previous studies in the following way. First, to minimize selection bias, we select AGNs that fall below the knee of the black hole mass function. Second, we estimate \mathcal{M}_{BH} using Balmer lines which avoids potential systematic uncertainties in the UV-based estimators. Third, our X-ray selected sample have lower nuclear-to-host ratios which facilitate the galaxy mass measurements. Moreover, 21/32 systems in our sample have two-band *HST* data (i.e. WFC3+ACS), whose multi-band information provides reliable K-correction and stellar mass inference. Given the high-quality of our data, we can test whether the growth of BH predates that of the host by a factor of at least 1.7 (~ 0.23 dex) [what does this mean?].

The paper is organized as follows. We briefly describe the sample selection and the BH mass of the sample in Section 2. We describe the observation and collect the PSF library in Section 3. In Section 4 we decompose our sample and study the host galaxy surface photometry. In Section 5, we use the multi-band host magnitudes to infer their stellar population, which we applied to derive the rest-frame R band L_{host} and M_* and compared to the local samples. Discussion and conclusion are presented in Section 6 and Section 7.

Throughout this paper, we adopt a standard concordance cosmology with $H_0 = 70 \text{ km s}^{-1} \text{ Mpc}^{-1}$, $\Omega_m = 0.30$, and $\Omega_\Lambda = 0.70$. Magnitudes are given in the AB system.

2. SAMPLE SELECTION AND \mathcal{M}_{BH}

We focus on the broad-line (type-1) AGNs as provided by the X-ray coverage of COSMOS (Civano et al. 2016), (E)-CDFS-S (Lehmer et al. 2005; Xue et al. 2011), and SXDS (Ueda et al. 2008) fields. We select the broad-line AGNs at redshift region $1.2 < z < 1.7$ which cover a BH range $7.5 < \log \mathcal{M}_{\text{BH}} < 8.5$. The Near IR spectra of AGNs are available from the survey of Subaru's Fiber Multi-Object Spectrograph (FMOS, Kimura et al. 2010; Schulze et al. 2018), covering the wavelength range $0.9\text{--}1.8 \mu\text{m}$. The FMOS survey provides the best \mathcal{M}_{BH} estimates by $H\alpha$ and $H\beta$ lines out to $z \sim 1.7$ (Greene & Ho 2005; Matsuoka et al. 2013; Nobuta et al. 2012). Overall, our final sample is composed of 32 new observations by *HST*/WFC3. Table 1 list all the AGN systems analyzed in this work.

The \mathcal{M}_{BH} of type-1 AGNs can be inferred using the so-called virial method (Peterson et al. 2004; Shen 2013). The kinematics of the broad-line region (BLR) trace the gravita-

tional field of the central supermassive black hole, assuming the gravity dominates the motion of the BLR gas. In this scenario, the width of the emission-line provided the scale of the velocity, while the AGN continuum luminosity establish an empirical scale of the BLR size. As a result, the estimation of the \mathcal{M}_{BH} is achieved by these measurements.

For our targets, the $H\alpha$ and $H\beta$ emission-line properties have been investigated by Schulze et al. (2018) using the multi-object spectrograph Subaru/FMOS. We referred to that paper for the details of continuum fitting and emission line modeling. Since the other compared AGNs in the literature used different calibrations of the virial method, we compare the difference among the recipes by Schulze et al. (2018); McGill et al. (2008); Ding et al. (2017b) and adopt a list of consistent ones to cross-calibrate the \mathcal{M}_{BH} for all the samples, in order to avoid any systematic bias in Section 2.2.

2.1. Comparison sample

We aim to collect the $\mathcal{M}_{\text{BH}}\text{--}L_{\text{host}}$ and $\mathcal{M}_{\text{BH}}\text{--}M_*$ relations of our samples and comparing to the ones at different redshift. For comparison with the local relation, we use the local AGN measurements by Bennert et al. (2010) and Bennert et al. (2011a) (hereafter, B10 and B11a) to define our zero-point. The sample by B10 consists of 19 $\mathcal{M}_{\text{BH}}\text{--}L_{\text{host}}$ measured with reliable \mathcal{M}_{BH} measured using reverberation-mapped (uncertainty level ~ 0.15 dex). The work of B11 contains 25 $\mathcal{M}_{\text{BH}}\text{--}M_*$ local active AGNs, where the \mathcal{M}_{BH} are measured from the single-epoch method (\mathcal{M}_{BH} uncertainty level ~ 0.4 dex). To increase the local M_* and \mathcal{M}_{BH} to the higher range, we also include the inactive galaxies (mainly ellipticals or S0) as done by Häring & Rix (2004). It is worth noting that in the local comparison sample, the bulge mass is equivalent to the total stellar mass for the local comparison sample. In other words, our local comparison is the $\mathcal{M}_{\text{BH}}\text{--}M_{* \text{ Bulge}}$ and not those involving total quantities.

We include in our analysis published samples at intermediate redshift range to understand the redshift evolution of these correlations. We select samples that were analyzed by members of our team, in order to ensure uniform measurements. The intermediate redshift AGNs that we consider include, for the $\mathcal{M}_{\text{BH}}\text{--}L_{\text{host}}$ relation, 52 objects published by Park et al. (2015) at $0.36 < z < 0.57$ and 27 objects published by Bennert et al. (2011b); Schramm & Silverman (2013) at $0.5 < z < 1.9$. Moreover, Schramm & Silverman (2013) also derive the M_* which enable us to compare to the $\mathcal{M}_{\text{BH}}\text{--}M_*$ relation at $0.5 < z < 1.2$.

2.2. BH masses

To avoid any systematic bias between our samples and the literature ones, we compared the recipes as introduced by Schulze et al. (2018); Ding et al. (2017b). We find that the $H\beta$ estimator is very consistent (< 0.03 dex r.m.s. or mean?) between the two references. Moreover, in Schulze et al. (2018), the cross-calibration between the $H\alpha$ and $H\beta$ is consistent. Thus, we adopt the virial formalism from Schulze et al. (2018):

$$\log \left(\frac{\mathcal{M}_{\text{BH}}(H\alpha)}{M_\odot} \right) = 6.71 + 0.48 \log \left(\frac{\lambda L_{H\alpha}}{10^{42} \text{ erg s}^{-1}} \right) + 2.12 \log \left(\frac{\text{FWHM}(H\alpha)}{1000 \text{ km s}^{-1}} \right). \quad (1)$$

and

$$\log\left(\frac{\mathcal{M}_{\text{BH}}(H\beta)}{M_{\odot}}\right) = 6.91 + 0.50 \log\left(\frac{\lambda L_{\lambda_{5100}}}{10^{44} \text{ erg s}^{-1}}\right) + 2.0 \log\left(\frac{\text{FWHM}(5100)}{1000 \text{ km s}^{-1}}\right), \quad (2)$$

Having defined the recipes, we estimate \mathcal{M}_{BH} by adopting the emission line properties measured by [Schulze et al. \(2018\)](#). 14 of the systems have both $H\alpha$ and $H\beta$ emission line information; we adopt the averaged \mathcal{M}_{BH} value. We summarized the inference of the \mathcal{M}_{BH} together with the properties of the emission line in Table 4.

3. HST OBSERVATIONS

High spatial resolution imaging is required for the decomposition of the nuclear/host emission and the accurate estimate of the host stellar mass. For this purpose, all the new 32 AGN systems were observed with the HST/WFC3 infrared channel, as part of the HST program GO-15115, PI: John Silverman. We selected to use the filters F125W ($1.2 < z < 1.44$) and F140W ($1.44 < z < 1.7$) according to the redshift of the targets. This selection ensures that the broad $H\alpha$ line is not present in the bandpass so as not to contaminate the host emissions due to the broad wings of the PSF.

For each of the 32 new AGNs we obtained six separate exposures with $\sim 399s$ (i.e. total exposure time $\sim 2394s$). Table 1 lists the details of the observation. The six exposures for each dither image were combined with the ASTRODRIZZLE software package, with an output pixel scale of $0''.0642$ by setting `pixfrac` parameter as 0.8 using the `gaussian` kernel. To accurately estimate the background light which could come from both the sky and the detector, we adopt the `PHOTUTILS` tool.

Multi-band information provides the spectral energy distributions (SED) at a more precise level. 21/32 objects in our sample have rest-frame UV images by [Scoville et al. \(2007\)](#). Images were taken through the wide ACS/F814W filter at four dither pointing with 507s exposures. The final image is drizzled to $0''.03$ pixel scale. Given the multi-band image for these systems, we are able to infer their host color and assess the contribution of both the young and old stellar population to the stellar mass budget [Gallazzi & Bell \(2009\)](#) which insures an accurate inference of rest-frame R-band luminosity by K-correction, stellar mass and star formation rate (SFR).

3.1. PSF library

The knowledge of the PSF is crucial for the AGN imaging decomposition, especially when the point source is bright relative to the host. The PSF is known to be vary across the detector and with time, due to the effects of aberrations and breathing. Simulated PSF, such as TINYTIM ones, are usually insufficient matches to observations for our purposes [Mechtley et al. \(2012\)](#). Stars within the fields provide a better description than the simulated PSF, since they were observed simultaneously with the science targets and reduced and analyzed in the same way [Kim et al. \(2008\)](#); [Park et al. \(2015\)](#).

To minimize the impact of the mismatch, we build a PSF library by selecting all the isolated, unsaturated PSF-stars with high S/N from our entire program. The selection consists of the following steps. We first adopt the identified stars as candidates from the COSMOS2015 catalog by [Laigle et al. \(2016\)](#). A lot of bright stars with intensity similar to the AGNs

were excluded by [Laigle et al. \(2016\)](#); in the second step, we manually select the PSF-like objects as candidates. We then remove the non-ideal PSF candidates based on their intensity, FWHM, central symmetry and any that were contaminated by nearby objects. In the end, the PSF library contains 78 and 37 PSFs imaged through filters F140W and F125W, respectively.

We assume that the stars in the library are representative of the possible PSFs in our program. Therefore, we assume that the PSF library gives a good representation of the dominant source of uncertainty as well as the best fit.

4. AGN-HOST DECOMPOSITION

We simultaneously fit the two-dimensional flux distribution of the center nuclear and the underlying host galaxy. Following common practice, we assume the unresolved nuclear as a scaled point source, while the host galaxy as a Sérsic profile. Note that the actual morphologies of the host galaxies could be more complicated (e.g. bulge+disk). However, the purpose of adopting the Sérsic model is a simplified a first-order approximation of the surface brightness distribution with a flexible parameterization which provides sufficient freedom to infer the host flux, given the high redshift range of our sample. Furthermore, we fit other galaxies that happen to be close to the AGN as additional Sérsic model, to account for any potential contamination. [The systems CID206 and ECDFS-358 have nearby objects which could not be described by Sérsic model, we thus mask these objects in the fitting.](#)

We adopt the imaging modeling tool LENSTRONOMY ([Birrer & Amara 2018](#)) to perform the decomposition of the host and nuclear light. LENSTRONOMY is a multi-purpose open-source gravitational lens image modeling python package. Its flexibility enables us to turn off the lensing channel and focus on the AGN decomposition⁷. The main advantage over GALFIT is that LENSTRONOMY returns the full posterior of the parameter and not just the best fit model and the Laplace approximation of the uncertainties. The input ingredients to LENSTRONOMY include:

1. AGN imaging data.
 - Using aperture photometry, we find that an aperture size with radius $\sim 1''.5$ covers sufficient AGN light our samples. By default, we cut out the AGN image to a 61×61 pixels box (i.e. $4'' \times 4''$). If needed, the larger size box would be sufficient to include the nearby objects.
2. Noise level map.
 - The origin of the noise in each pixel stems from the read noise, background noise and Poisson noise by the astronomical sources themselves. To take them into account, we measure the read noise and background noise level directly from the empty regions of the data. We calculate the effective exposure time of each pixel based on the drizzled WHT array maps to infer the Poisson noise level.
3. PSF.
 - The PSF is directly taken from the PSF library. Usually, a mismatch exists when subtracting the AGN as the

⁷ For a sanity check, we compared the performance of LENSTRONOMY to the most commonly used galaxy modeling software GALFIT and confirm that the consistent result could be obtained with the same fitting ingredients provided.

scaled PSF, especially at the central parts. While modeling multiply imaged AGN, this mismatch can be mitigated with PSF reconstruction by the iterative method (Chen et al. 2016; Birrer et al. 2018). However, this approach requires multiple images which are not available in our case. We remedy this deficiency by using a broad library which should contain sufficient information to cover all the possible PSF.

The host properties of one AGN system is inferred via the following steps. First, we model the AGN and host using each PSFs in the library. Inputting the fitting ingredients to LENSTRONOMY, the posterior distribution of the parameter space is calculated and optimized by adopting the Particle Swarm Optimizer (PSO)⁸. To avoid any unphysical inferences, we set the upper and lower limit for the key parameters as effective radius $R_{\text{eff}} \in [0''.1, 1'']$, and Sérsic index $n \in [1, 7]$. Then, we rank the performance of each PSF based on the χ^2 value and select the top-eight PSFs as representative of the best fit PSFs. We infer the host property (i.e., host flux, R_{eff} , Sérsic index n) using a weighted arithmetic mean. The weight is calculated by:

$$w_i = \exp\left(-\alpha \frac{(\chi_i^2 - \chi_{\text{best}}^2)}{2\chi_{\text{best}}^2}\right), \quad (3)$$

where the α is an inflation parameter so that when $i = 8$:

$$\alpha \frac{\chi_{i=8}^2 - \chi_{\text{best}}^2}{2\chi_{\text{best}}^2} = 2, \quad (4)$$

The goal of this recipe is to weight each PSF based on their relative goodness of fit, while ensuring at least eight are used to capture the range of systematic uncertainties. The answers would not change significantly if we had chosen a different number of PSFs, as we show below.

Note that since each AGN system was observed in different location of the detector and at a different time, the top-eight PSFs usually vary from one AGN system to another. Given the weights, the inferred value of host properties and the root-mean-square (σ) are calculated as:

$$\bar{x} = \frac{\sum_{i=1}^8 x_i * w_i}{\sum w_i}, \quad (5)$$

$$\sigma = \sqrt{\frac{\sum_{i=1}^8 (x_i - \bar{x})^2 * w_i}{\sum w_i}}. \quad (6)$$

In Figure 1, we demonstrate the optimized results inferred by LENSTRONOMY, including the AGN images, best-fit models, image subtract point source (i.e. host) and the residuals. As an example, the weights adopted in the analysis of system COSMOS-CID1174 are listed in Table 2. In order to quickly overview our inference, we summarize the relations of the properties between effective radius R_{eff} , 2) Sérsic index n and 3) host to total flux ratio in Figure 2.

The inference of the host properties is weighted by eight top-ranked PSFs. For a smaller number of PSFs one tends to underestimate the uncertainties. To understand how the choice of the number of top-ranked PSF affects our inference,

⁸ Note that, the LENSTRONOMY enables one to further infer the parametric confidence interval using MCMC. However, in our case, given a fixed PSF, the $1 - \sigma$ inference of each parameter are extremely narrow.

we compare to the one inferred by five and ten top-ranked PSFs. As shown in Figure 3, the results are very consistent, meaning that the host inference is solid when the amount of selected PSF exceeds five.

18/32 systems in the COSMOS field have ACS/F184W imaging data. We infer their host properties using the same approach used for the WFC3-IR data. The field of view by ACS are larger than WFC3, and we collected in total 174 ACS PSFs in the library. In principle, the host inference by IR band is superior to the one by UV band, giving that the effects of dust extinction and contrast between the (blue) AGN and (red) host. Thus, we fix the R_{eff} and Sérsic n as the value inferred by IR band, assuming that the morphology of the galaxy is consistent between ACS and WFC3.

We list all the inference of the host galaxy properties in the Table 3.

5. RESULTS

5.1. Host galaxy properties

We derive the rest-frame R band magnitude (M_R) and luminosity (L_R) of our sample based on their filter magnitude. 18/32 systems have multi-band host magnitude which enables us to select the best stellar population that could fit the overall sample. We find that the 1 Gyr stellar population with solar metallicity by Chabrier initial mass function (IMF) (Bruzual & Charlot 2003) could well match the color between the WFC3 and ACS band magnitude of these samples. Adopting the color information, we perform the K-correction and derive the rest-frame R band magnitude of our sample. Given that the WFC3 filter we selected is very close to the rest-frame R band, we expect the M_R uncertainty introduced by this K-correction is within 0.05 mag. We derive the rest-frame R band luminosity by $\log L_R/L_{R,\odot} = 0.4(M_{R,\odot} - M_R)$, where $M_{R,\odot} = 4.61$ (Blanton & Roweis 2007).

Taking the stellar population, we estimate the stellar mass content of each host galaxy according to the mass-to-light ratio of the stellar population we adopted. The uncertainty level associated with the stellar mass is expected to be of order 0.1 dex, at fixed stellar initial mass function (changing the initial mass function would change all our stellar masses systematically).

The inferred L_R and M_* are listed in Table 3. In the rest of this section, we compare their relations to to the \mathcal{M}_{BH} .

5.2. $\mathcal{M}_{\text{BH}}-L_{\text{host}}$ relation

We show our measurements of the $\mathcal{M}_{\text{BH}}-L_{\text{host}}$ relation together with the comparison sample in Figure 4, panel (a). Following common practice, we fit the local relation as a linear relation,

$$\log\left(\frac{\mathcal{M}_{\text{BH}}}{10^7 M_\odot}\right) = \alpha + \beta \log\left(\frac{L_R}{10^{10} L_\odot}\right), \quad (7)$$

which enables direct comparison to the distant sample. The figure shows that the observed $\mathcal{M}_{\text{BH}}-L_{\text{host}}$ relation for our measurements is nearly identical to the local and intermediate ones, indicating that the black hole mass and the host luminosity located at a similar relation at different galaxy age. However, considering that both the black hole and host galaxy are expected to evolve over cosmic time, it is essential to transfer high- z measurements to their values at today so as to compare them in an equivalent frame. Especially, in a passive evolution scenario, we expect L_{host} to fade over time.

We follow [Ding et al. \(2017b\)](#) and parametrize the luminosity evolution with the functional form as $d\text{mag}_R \sim d\log(1+z)$, i.e.,

$$\log(L_{R,0}) = \log(L_R) - 1.48 \log(1+z). \quad (8)$$

This formalism is more accurate to fit a broad range redshift comparing to a single slope as $d\text{mag}/dz$. We refer to [Ding et al. \(2017b, section 5.4\)](#) for more details. Transferring the L_{host} to today, we show the evolution-corrected $\mathcal{M}_{\text{BH}}-L_{\text{host}}$ relation in Figure 4, panel (b) and find that, at fixed \mathcal{M}_{BH} , the BH in the more distant universe tends to reside in less luminous hosts.

To quantitatively understand this trend, we fit the offset as a function of redshift in form as:

$$\Delta \log \mathcal{M}_{\text{BH}} = \gamma \log(1+z), \quad (9)$$

where $\Delta \log \mathcal{M}_{\text{BH}} = \log(\frac{\mathcal{M}_{\text{BH}}}{10^7 M_\odot}) - \alpha - \beta \log(\frac{L_{R,0}}{10^{10} L_\odot})$. The best-fit and 1- σ inference are $\gamma = 0.69 \pm 0.15$.

Given that the current result does not take into account selection effects yet, we will draw the conclusion in section 5.4.

5.3. $\mathcal{M}_{\text{BH}}-M_*$ relation

Analyzing the correlation of the $\mathcal{M}_{\text{BH}}-M_*$ would be more efficient to help directly understand the connection between their coevolution. In Figure 6, we plot the $\mathcal{M}_{\text{BH}}-M_*$ relation and compare to the local and intermediate sample. We visually see that the mass distributions for the three samples are very similar. Similarly, we consider the local as linear relation to fit offset (i.e., $\Delta \log \mathcal{M}_{\text{BH}}$) as a function of $\gamma \log(1+z)$. We obtain the $\gamma = 0.49 \pm 0.19$, i.e. tentative evidence for evolution, see Figure 7, panel (a). We also show the ratio of $\mathcal{M}_{\text{BH}}-M_*$ of the three samples at different redshift in Figure 7, panel (b). We highlight that our results are less biased in both the measurement of \mathcal{M}_{BH} and M_* .

We highlight that the local sample employed are bulge-dominated galaxies and the adopted M_* are equivalent to their bulge masses. That is, we are comparing the $\mathcal{M}_{\text{BH}}-M_{*,\text{total}}$ at the distant universe to the $\mathcal{M}_{\text{BH}}-M_{*,\text{bulge}}$ at the local. Considering that a major part of the distant systems has indicated the disk component (i.e., the systems with fitted Sérsic index close to 1), the $M_{*,\text{bulge}}$ of them are supposed to be even less.

Without taking into account the selection effect, the direct comparison shows that the growth of the black hole predates that of the host bulge.

5.4. Selection effect

To be written after Daeseong's analysis..

6. DISCUSSION

6.1. Systematic error

In our analysis, we adopt one stellar population to the overall sample. We note that adopting the private stellar populations for these samples which have both multi-band host mag-

nitude could be more robust in principle. However, considering that the host magnitude in ACS band is faint (host-total flux ratio $< 30\%$), the fidelity of the SED fitting is actually lost. Perhaps the best way to derive the stellar population is to combining our measurements to the ground-based photometry. **Describe the ground-based data.** In this paper, we focus on the decomposing of the AGN and carry out a rapid analysis of the \mathcal{M}_{BH} -host relations. The measurements incorporating the ground-based photometry and the comparison with the simulations are presented in our companion paper.

6.2. Comparison to the inactive galaxies

We compared the morphology of AGNs host galaxies to the inactive galaxies in CANDLES imaging survey. We select 4401 inactive galaxies in a comparable redshift range ($1.2 < z < 1.7$) whose Sérsic properties are inferred by [van der Wel et al. \(2012\)](#) by GALFIT, and their stellar masses are derived by 3-D-HST spectroscopic survey ([Momcheva et al. 2016; Brammer et al. 2012](#)).

In Figure 8, we plot the M_* versus the R_{eff} and Sérsic index. The color coding is based on the filter flux ratio between WFC3 and ACS. The distribution of M_*-R_{eff} relation show that our AGN hosts concentrate at the high end of the stellar mass, close to the red sequence.

We also compare the histogram of the inferred R_{eff} and Sérsic n to the inactive galaxies in Figure 9, where there is no significant difference between their distribution and median value. We perform the Kolmogorov-Smirnov test to interpret the p-value as 0.42 and 0.04 for R_{eff} and n , respectively. We thus conclude that the host galaxies of our AGN are representative of the overall population of galaxies at comparable luminosity and stellar mass at the same redshift.

6.3. JWST

7. SUMMARY

ACKNOWLEDGMENTS

Based in part on observations made with the NASA/ESA Hubble Space Telescope, obtained at the Space Telescope Science Institute, which is operated by the Association of Universities for Research in Astronomy, Inc., under NASA contract NAS 5-26555. These observations are associated with programs #15115. Support for this work was provided by NASA through grant number HST-GO-15115 from the Space Telescope Science Institute, which is operated by AURA, Inc., under NASA contract NAS 5-26555.

The authors fully appreciate the discussions with Vardha N. Bennert, Takahiro Morishita.

XD and TT acknowledge support by the Packard Foundation through a Packard Research fellowship to TT.

This work has made use of lenstronomy ([Birrer & Amara 2018](#)), Astropy ([Astropy Collaboration et al. 2013](#)), photutils, TOPCAT ([Taylor 2005](#)), Matplotlib ([Hunter 2007](#)) and standard Python libraries.

REFERENCES

- Aird, J., Coil, A. L., Georgakakis, A., et al. 2015, MNRAS, 451, 1892 **1**
 Astropy Collaboration, Robitaille, T. P., Tollerud, E. J., et al. 2013, A&A, 558, A33 **7**
 Baskin, A., & Laor, A. 2005, MNRAS, 356, 1029 **1**
 Beifiori, A., Courteau, S., Corsini, E. M., & Zhu, Y. 2012, MNRAS, 419, 2497 **1**
 Bennert, V. N., Auger, M. W., Treu, T., Woo, J.-H., & Malkan, M. A. 2011a, ApJ, 726, 59 **2.1**
 —. 2011b, ApJ, 742, 107 **1, 2.1**
 Bennert, V. N., Treu, T., Woo, J., et al. 2010, ApJ, 708, 1507 **2.1**
 Birrer, S., & Amara, A. 2018, Physics of the Dark Universe, 22, 189 **4, 7**
 Birrer, S., Treu, T., Rusu, C. E., et al. 2018, arXiv e-prints, arXiv:1809.01274 **3**
 Blanton, M. R., & Roweis, S. 2007, AJ, 133, 734 **5.1**
 Brammer, G. B., van Dokkum, P. G., Franx, M., et al. 2012, ApJS, 200, 13 **6.2**

TABLE 1
DETAILS OF OBSERVATION

Object ID (1)	z (2)	WFC3/Filter (3)	RA (4)	DEC (5)	Observing date (6)	Expoure time (s) (7)
COSMOS-CID1174	1.552	F140W	150.2789	1.9595	2017-10-26	2395.4
COSMOS-CID1281	1.445	F140W	150.4160	2.5258	2018-11-26	2395.4
COSMOS-CID206	1.483	F140W	149.8371	2.0088	2017-10-23	2395.4
COSMOS-CID216	1.567	F140W	149.7918	1.8729	2017-10-23	2395.4
COSMOS-CID237	1.618	F140W	149.9916	1.7243	2018-06-03	2395.4
COSMOS-CID255 ^a	1.664	F140W	150.1017	1.8483	2019-03-16	2395.4
COSMOS-CID3242	1.532	F140W	149.7113	2.1452	2017-10-26	2395.4
COSMOS-CID3570	1.244	F125W	149.6411	2.1076	2017-10-27	2395.4
COSMOS-CID452	1.407	F125W	150.0045	2.2371	2017-10-25	2395.4
COSMOS-CID454	1.478	F140W	149.8681	2.3307	2018-02-26	2395.4
COSMOS-CID50	1.239	F125W	150.2080	2.0833	2017-10-23	2395.4
COSMOS-CID543	1.301	F125W	150.4519	2.1448	2018-04-30	2395.4
COSMOS-CID597	1.272	F125W	150.5262	2.2449	2018-11-25	2395.4
COSMOS-CID607	1.294	F125W	150.6097	2.3231	2017-10-25	2395.4
COSMOS-CID70	1.667	F140W	150.4051	2.2701	2017-10-27	2395.4
COSMOS-LID1273	1.617	F140W	150.0565	1.6275	2017-10-31	2395.4
COSMOS-LID1538	1.527	F140W	150.6215	2.1588	2018-05-01	2395.4
COSMOS-LID360	1.579	F140W	150.1251	2.8617	2017-10-30	2395.4
COSMOS-XID2138	1.551	F140W	149.7036	2.5781	2017-11-01	2395.4
COSMOS-XID2202	1.516	F140W	150.6530	1.9969	2017-11-05	2395.4
COSMOS-XID2396	1.600	F140W	149.4779	2.6425	2017-11-12	2395.4
CDFS-1	1.630	F140W	52.8990	-27.8600	2018-04-03	2395.4
CDFS-229	1.326	F125W	53.0680	-27.6580	2018-04-04	2395.4
CDFS-321	1.570	F140W	53.0486	-27.6239	2018-08-18	2395.4
CDFS-724	1.337	F125W	53.2870	-27.6940	2018-04-05	2395.4
ECDFS-358	1.626	F140W	53.0850	-28.0370	2018-02-09	2395.4
SXDS-X1136	1.325	F125W	34.8925	-5.1498	2018-01-29	2395.4
SXDS-X50	1.411	F125W	34.0267	-5.0602	2018-03-01	2395.4
SXDS-X717	1.276	F125W	34.5400	-5.0334	2018-07-02	2395.4
SXDS-X735	1.447	F140W	34.5581	-4.8781	2017-11-14	2395.4
SXDS-X763	1.412	F125W	34.5849	-4.7864	2018-07-03	2395.4
SXDS-X969	1.585	F140W	34.7594	-5.4291	2018-07-02	2395.4

NOTE. — Column 1: Object field and ID. Column 2: Redshifts. Column 3: WFC3 filter. Note that the targets from the COSMOS field also have ACS/F814W imaging. Column 4 and 5: J2000 RA and DEC coordinates. Column 6: The observing start date.

^aFor CID255, 3/6 of the dither WFC3 images are corrupted. We analyze this sample by a same approach, taking the 3 available frames.

- Bruzual, G., & Charlot, S. 2003, MNRAS, 344, 1000 [5.1](#)
Chen, G. C.-F., Suyu, S. H., Wong, K. C., et al. 2016, MNRAS, 462, 3457 [3](#)
Cisternas, M., Jahnke, K., Bongiorno, A., et al. 2011, ApJ, 741, L11 [1](#)
Civano, F., Marchesi, S., Comastri, A., et al. 2016, ApJ, 819, 62 [2](#)
DeGraf, C., Di Matteo, T., Treu, T., et al. 2015, MNRAS, 454, 913 [1](#)
Di Matteo, T., Colberg, J., Springel, V., Hernquist, L., & Sijacki, D. 2008, ApJ, 676, 33 [1](#)
Ding, X., Liao, K., Treu, T., et al. 2017a, MNRAS, 465, 4634 [1](#)
Ding, X., Treu, T., Suyu, S. H., et al. 2017b, MNRAS, 472, 90 [1, 2, 2.2, 5.2,](#)
[5.2](#)
Ferrarese, L., & Merritt, D. 2000, ApJ, 539, L9 [1](#)
Gallazzi, A., & Bell, E. F. 2009, ApJS, 185, 253 [3](#)
Gebhardt, K., Bender, R., Bower, G., et al. 2001, ApJ, 555, L75 [1](#)
Graham, A. W., Onken, C. A., Athanassoula, E., & Combes, F. 2011, MNRAS, 412, 2211 [1](#)
Greene, J. E., & Ho, L. C. 2005, ApJ, 630, 122 [2](#)
Gültekin, K., Richstone, D. O., Gebhardt, K., et al. 2009, ApJ, 698, 198 [1](#)
Häring, N., & Rix, H.-W. 2004, ApJ, 604, L89 [1, 2.1](#)
Hirschmann, M., Khochfar, S., Burkert, A., et al. 2010, MNRAS, 407, 1016 [1](#)
Hopkins, P. F., Hernquist, L., Cox, T. J., & Kereš, D. 2008, ApJS, 175, 356 [1](#)
Hunter, J. D. 2007, Computing in Science and Engineering, 9, 90 [7](#)
Jahnke, K., & Macciò, A. V. 2011, ApJ, 734, 92 [1](#)
Jahnke, K., Bongiorno, A., Brusa, M., et al. 2009, ApJ, 706, L215 [1](#)
Kim, M., Ho, L. C., Peng, C. Y., Barth, A. J., & Im, M. 2008, ApJS, 179, 283 [3.1](#)
Kimura, M., Maihara, T., Iwamuro, F., et al. 2010, PASJ, 62, 1135 [2](#)
Laigle, C., McCracken, H. J., Ilbert, O., et al. 2016, ApJS, 224, 24 [3.1](#)
Lauer, T. R., Tremaine, S., Richstone, D., & Faber, S. M. 2007, ApJ, 670, 249 [1](#)
Lehmer, B. D., Brandt, W. N., Alexander, D. M., et al. 2005, ApJS, 161, 21 [2](#)
Magorrian, J., Tremaine, S., Richstone, D., et al. 1998, AJ, 115, 2285 [1](#)
Marconi, A., & Hunt, L. K. 2003, ApJ, 589, L21 [1](#)
Matsuoka, K., Silverman, J. D., Schramm, M., et al. 2013, ApJ, 771, 64 [2](#)
McGill, K. L., Woo, J., Treu, T., & Malkan, M. A. 2008, ApJ, 673, 703 [2](#)
Mechtley, M., Windhorst, R. A., Ryan, R. E., et al. 2012, ApJ, 756, L38 [3.1](#)
Momecheva, I. G., Brammer, G. B., van Dokkum, P. G., et al. 2016, ApJS, 225, 27 [6.2](#)
Nobuta, K., Akiyama, M., Ueda, Y., et al. 2012, ApJ, 761, 143 [2](#)
Park, D., Woo, J.-H., Bennert, V. N., et al. 2015, ApJ, 799, 164 [1, 2.1, 3.1](#)
Peng, C. Y. 2007, ApJ, 671, 1098 [1](#)
Peng, C. Y., Impey, C. D., Rix, H.-W., et al. 2006, ApJ, 649, 616 [1](#)
Peterson, B. M., Ferrarese, L., Gilbert, K. M., et al. 2004, ApJ, 613, 682 [2](#)
Salviander, S., Shields, G. A., Gebhardt, K., & Bonning, E. W. 2006, New Astronomy Review, 50, 803 [1](#)
Schramm, M., & Silverman, J. D. 2013, ApJ, 767, 13 [1, 2.1](#)
Schulze, A., & Wisotzki, L. 2011, A&A, 535, A87 [1](#)
—, 2014, MNRAS, 438, 3422 [1](#)
Schulze, A., Silverman, J. D., Kashino, D., et al. 2018, ArXiv e-prints, arXiv:1810.07445 [1, 2, 2.2, 2.2](#)
Scoville, N., Abraham, R. G., Aussel, H., et al. 2007, ApJS, 172, 38 [3](#)
Shen, Y. 2013, Bulletin of the Astronomical Society of India, 41, 61 [2](#)
Springel, V., White, S. D. M., Jenkins, A., et al. 2005, Nature, 435, 629 [1](#)
Sun, M., Trump, J. R., Brandt, W. N., et al. 2015, ApJ, 802, 14 [1](#)
Taylor, M. B. 2005, in Astronomical Society of the Pacific Conference Series, Vol. 347, Astronomical Data Analysis Software and Systems XIV, ed. P. Shopbell, M. Britton, & R. Ebert, 29 [7](#)
Trakhtenbrot, B., & Netzer, H. 2012, MNRAS, 427, 3081 [1](#)
Treu, T., Malkan, M. A., & Blandford, R. D. 2004, ApJ, 615, L97 [1](#)
Treu, T., Woo, J.-H., Malkan, M. A., & Blandford, R. D. 2007a, ApJ, 667, 117 [1](#)
—, 2007b, ApJ, 667, 117 [1](#)
Ueda, Y., Watson, M. G., Stewart, I. M., et al. 2008, ApJS, 179, 124 [2](#)
van der Wel, A., Bell, E. F., Häussler, B., et al. 2012, ApJS, 203, 24 [6.2](#)
Woo, J., Treu, T., Malkan, M. A., & Blandford, R. D. 2006, ApJ, 645, 900 [1](#)
Woo, J.-H., Treu, T., Malkan, M. A., & Blandford, R. D. 2008, ApJ, 681, 925 [1](#)
Xue, Y. Q., Luo, B., Brandt, W. N., et al. 2011, ApJS, 195, 10 [2](#)

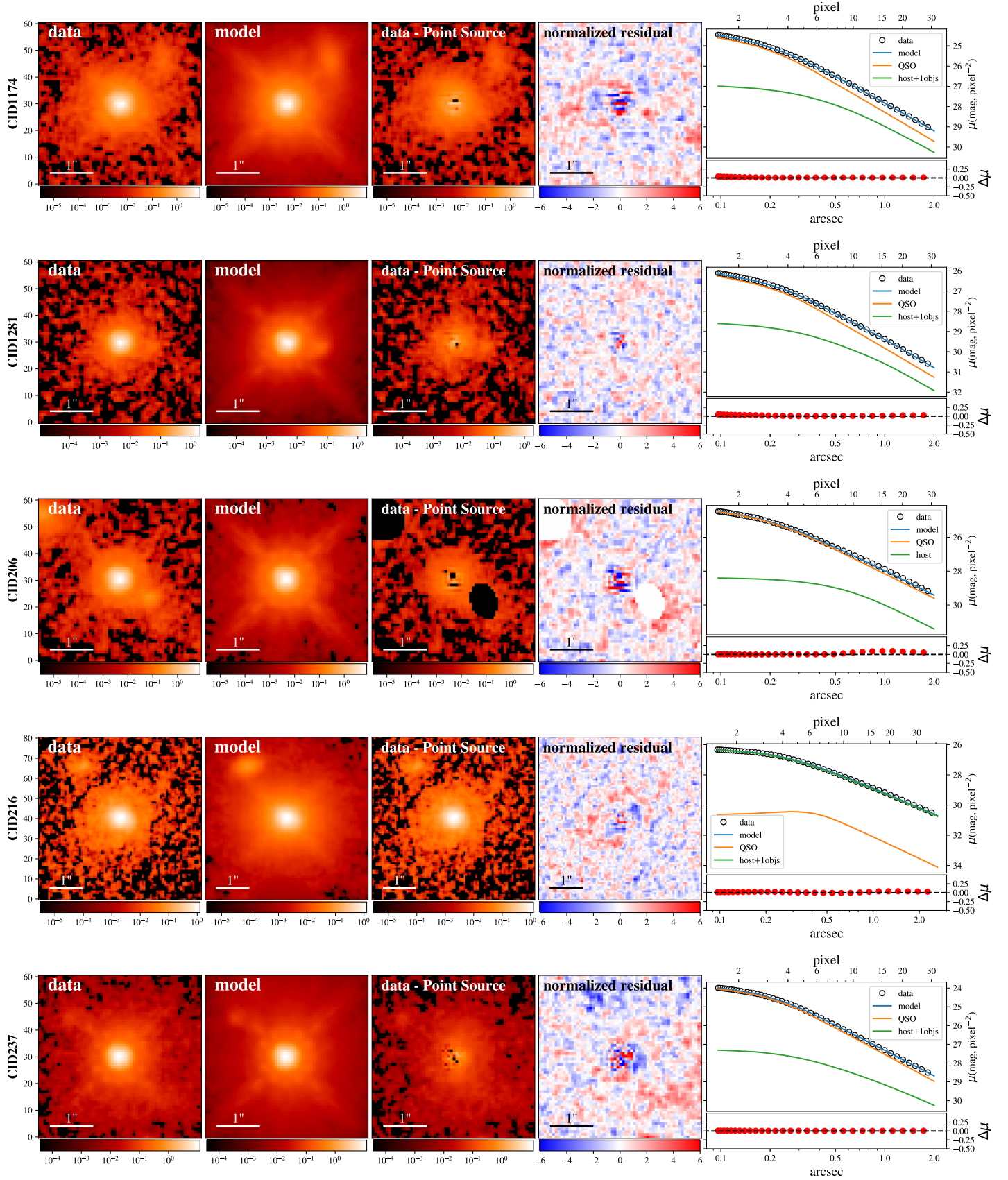


FIG. 1.— Figure illustrates the inference for the 32 objects based on the WFC3 images. In each row, observed data (first column), best-fit models (second column), data subtracted by the inferred point source (third column), normalized residuals (fourth column) are presented together with the target ID. In the fifth column, we present the 1-D surface brightness profiles (top) and the corresponding residual (bottom). The 1-D profiles indicate the surface brightness including the data (open circles), the best-fit model (blue line), the AGN (orange line), and the model for the extended sources (green line, i.e., host and other objects). Note that the one-dimensional surface brightness profiles are only for illustration purposes. The actual fitting is based on the two-dimensional images.

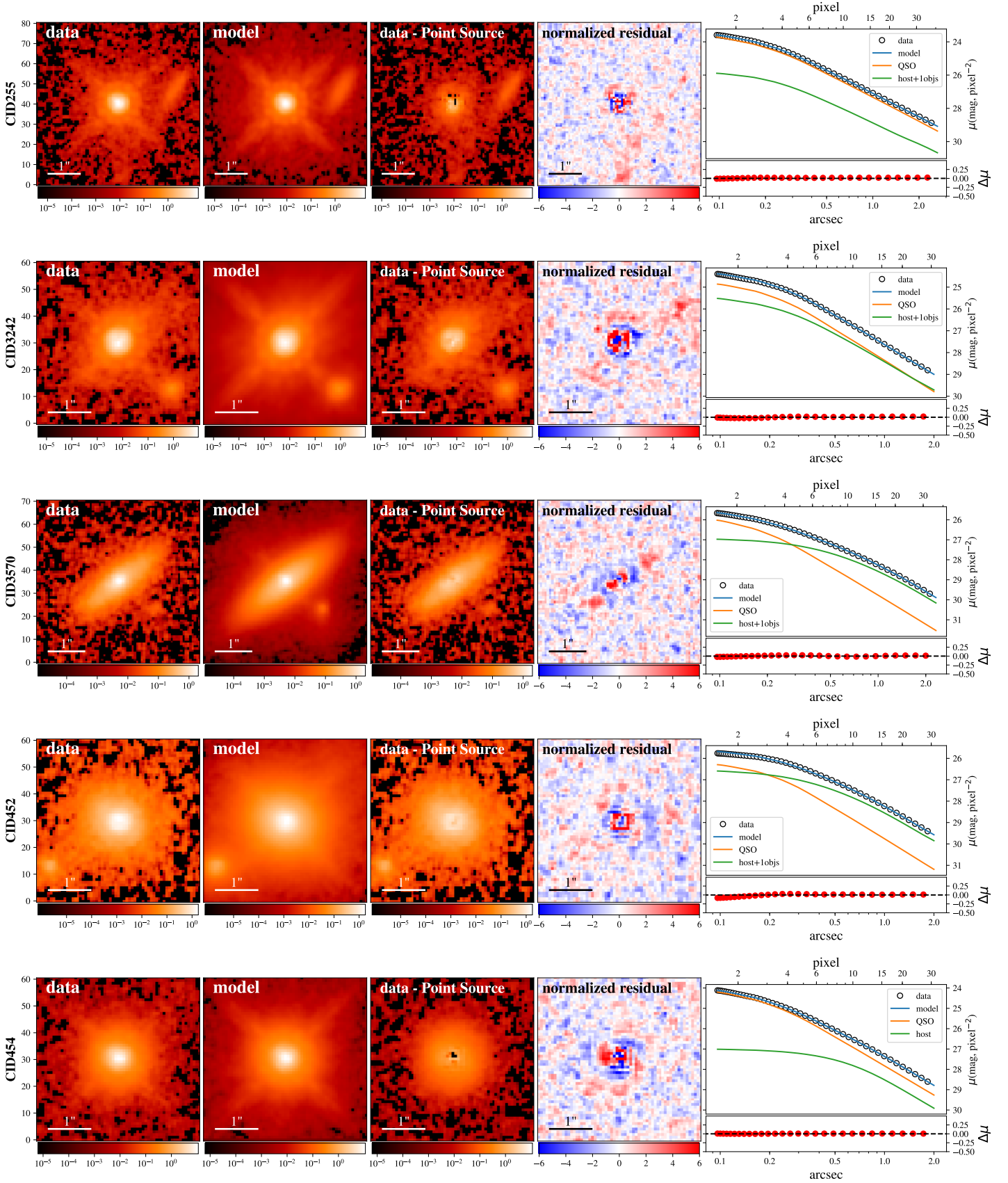


FIG. 1. — Continued.

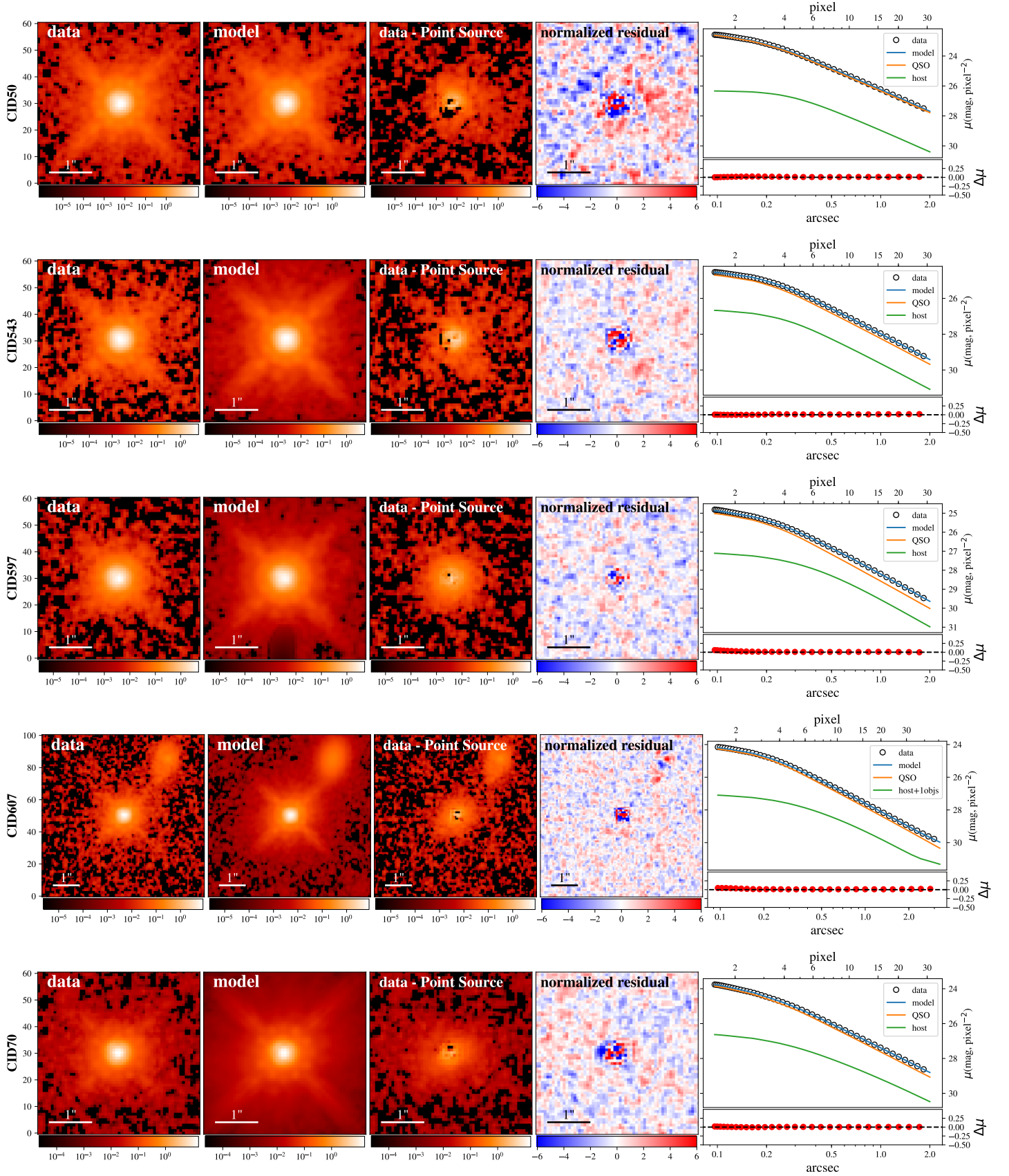


FIG. 1. — Continued.

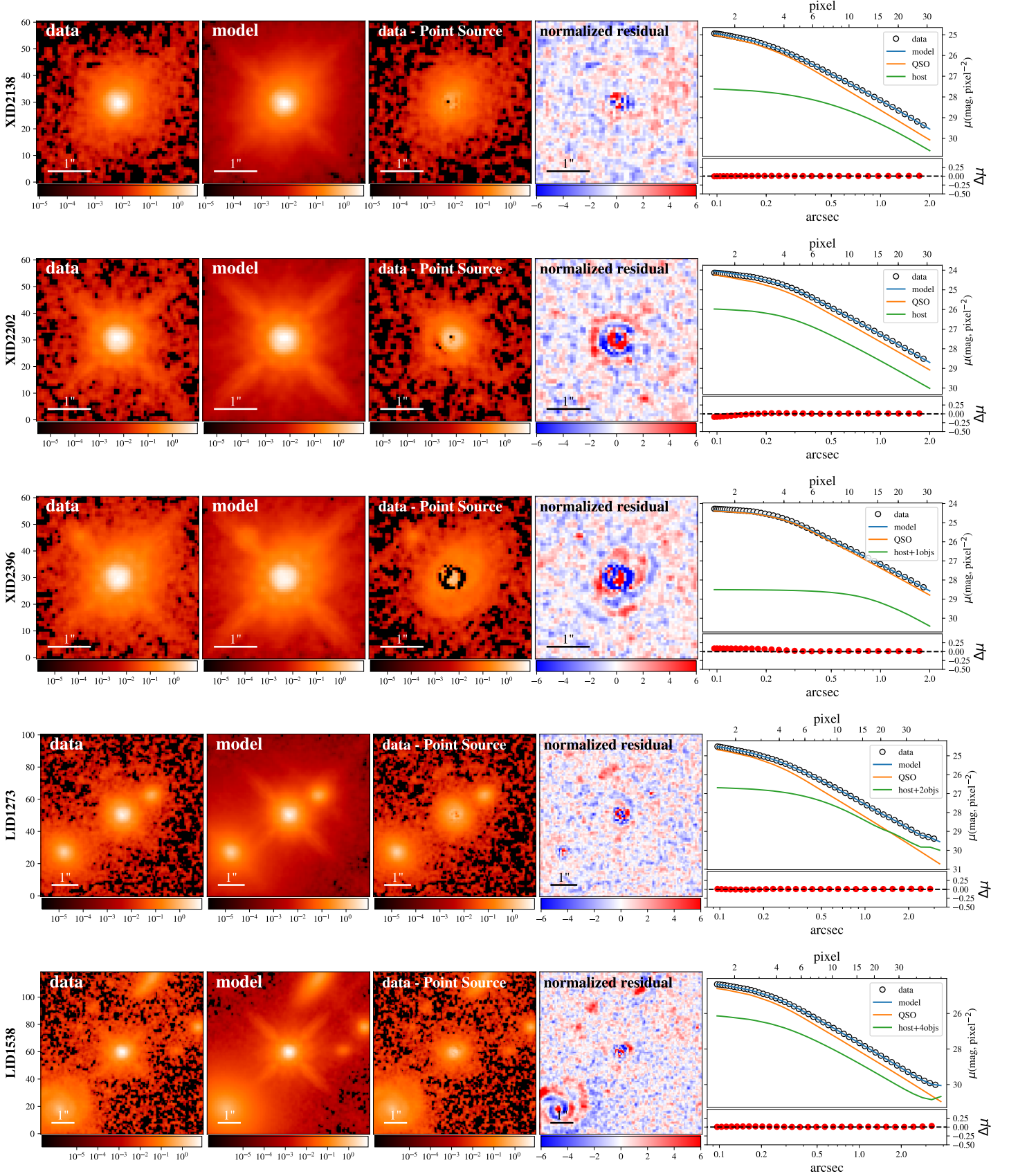


FIG. 1.— Continued.

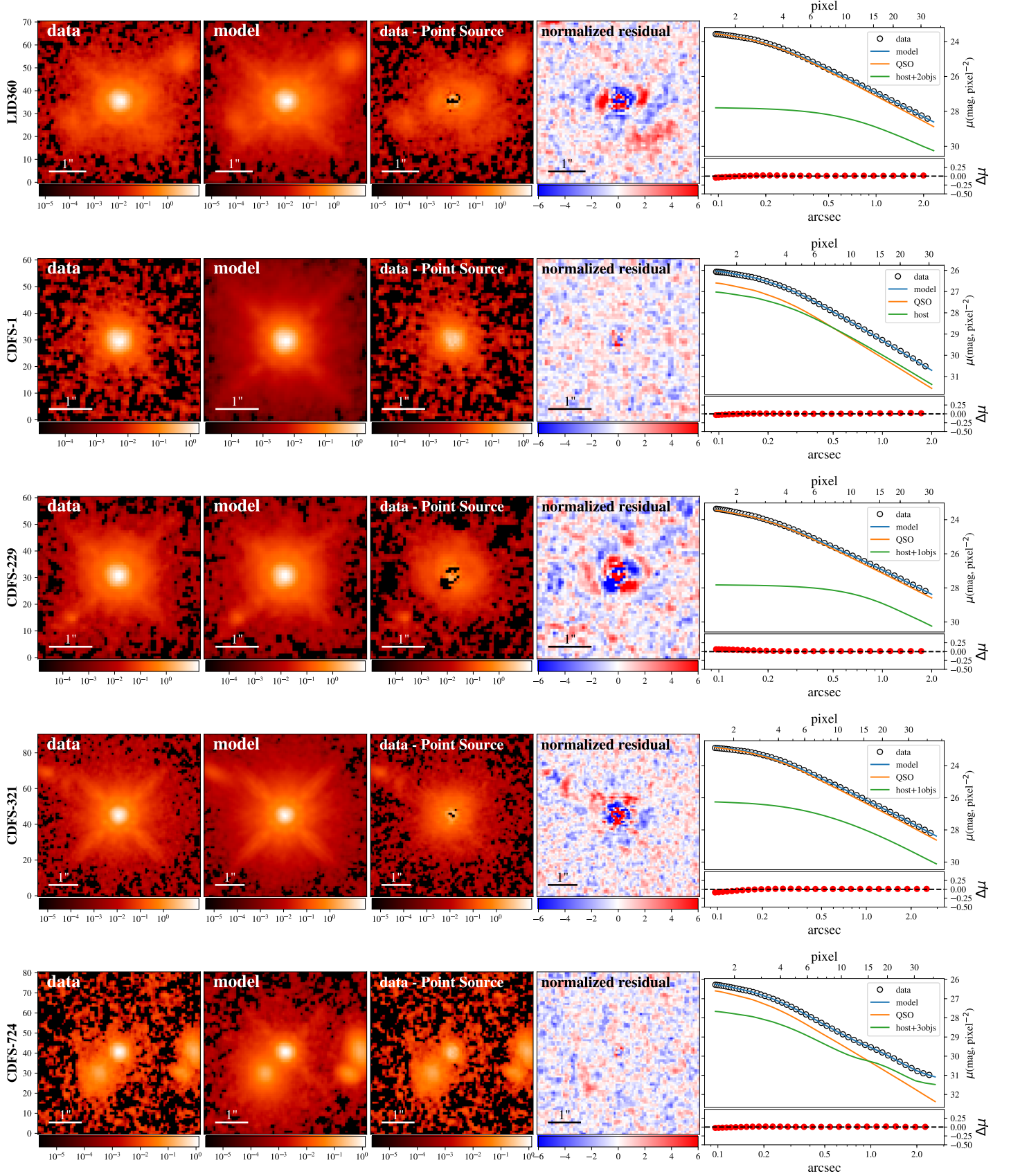


FIG. 1.— Continued.

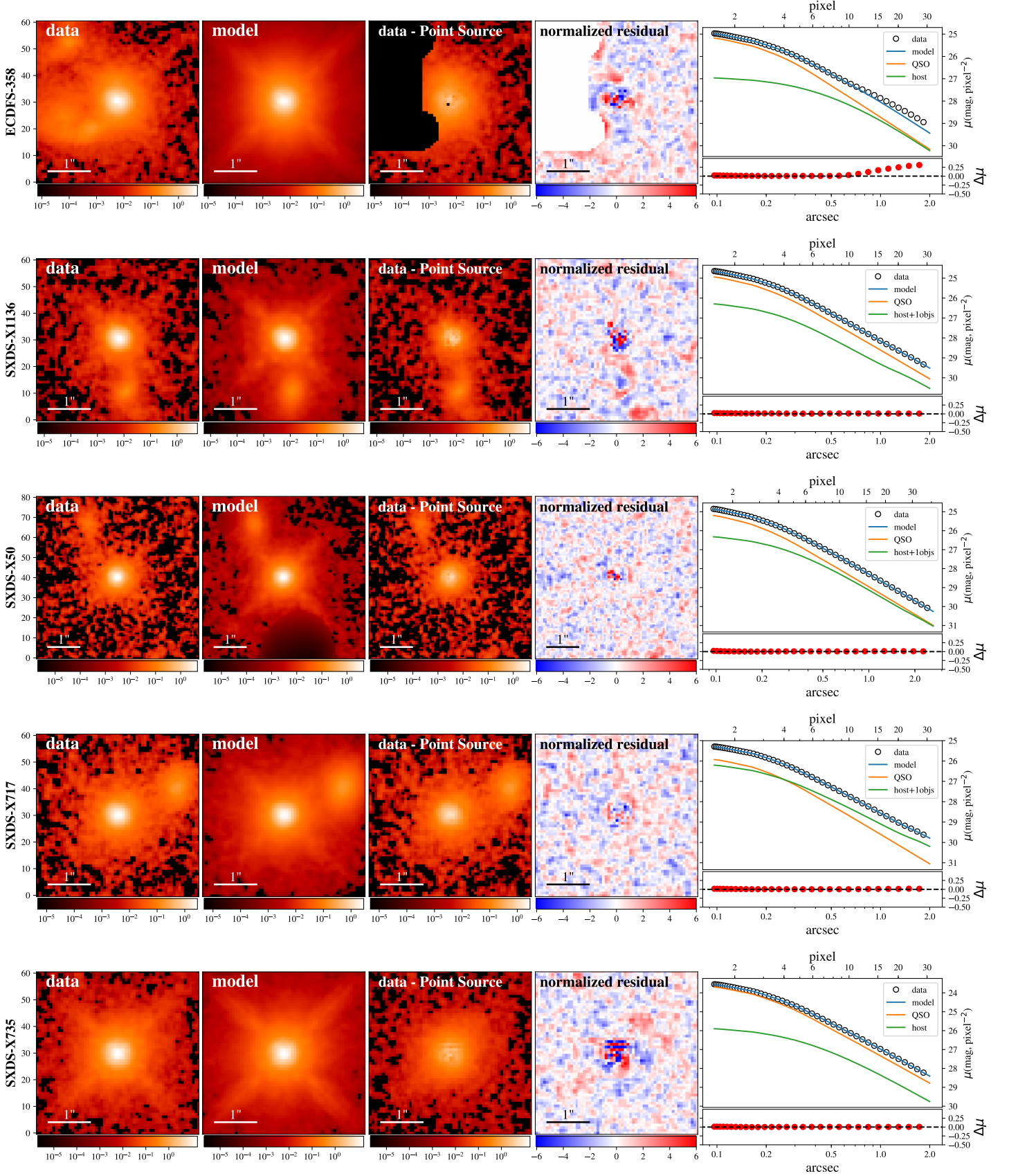


FIG. 1.— Continued.

TABLE 2
THE HOST INFERENCE OF CID1174

PSF rank (1)	total χ^2 (2)	weights w_i (3)	host flux (counts) (4)	host flux ratio (5)	R_{eff} (arcsec) (6)	Sérsic n (7)
1	8584.429	1.000	82.2	35%	$0''.345$	1.1
2	8646.711	0.920	99.1	42%	$0''.298$	1.9
3	8816.947	0.734	76.7	33%	$0''.365$	1.1
4	9304.841	0.383	128.6	55%	$0''.231$	2.8
5	9652.575	0.241	187.5	79%	$0''.116$	6.2
6	9917.101	0.170	100.2	42%	$0''.287$	2.1
7	10018.324	0.148	75.1	32%	$0''.365$	1.2
8	10087.456	0.135	79.8	34%	$0''.358$	1.2

Weighted value 97.322 ± 28.336 $42\% \pm 12\%$ $0''.309 \pm 0''.065$ 1.9 ± 1.3

NOTE. — Column 1: Rank of the PSF from the library. Column 2: Total χ^2 for the corresponding PSF. Column 3: Weights for the inference. Column 4-7: Fitted value for the host flux, host/total flux ratio, effective radius, and Sérsic index. For this sample, the inflation parameter α calculated by Eq. 4 is 16.671.

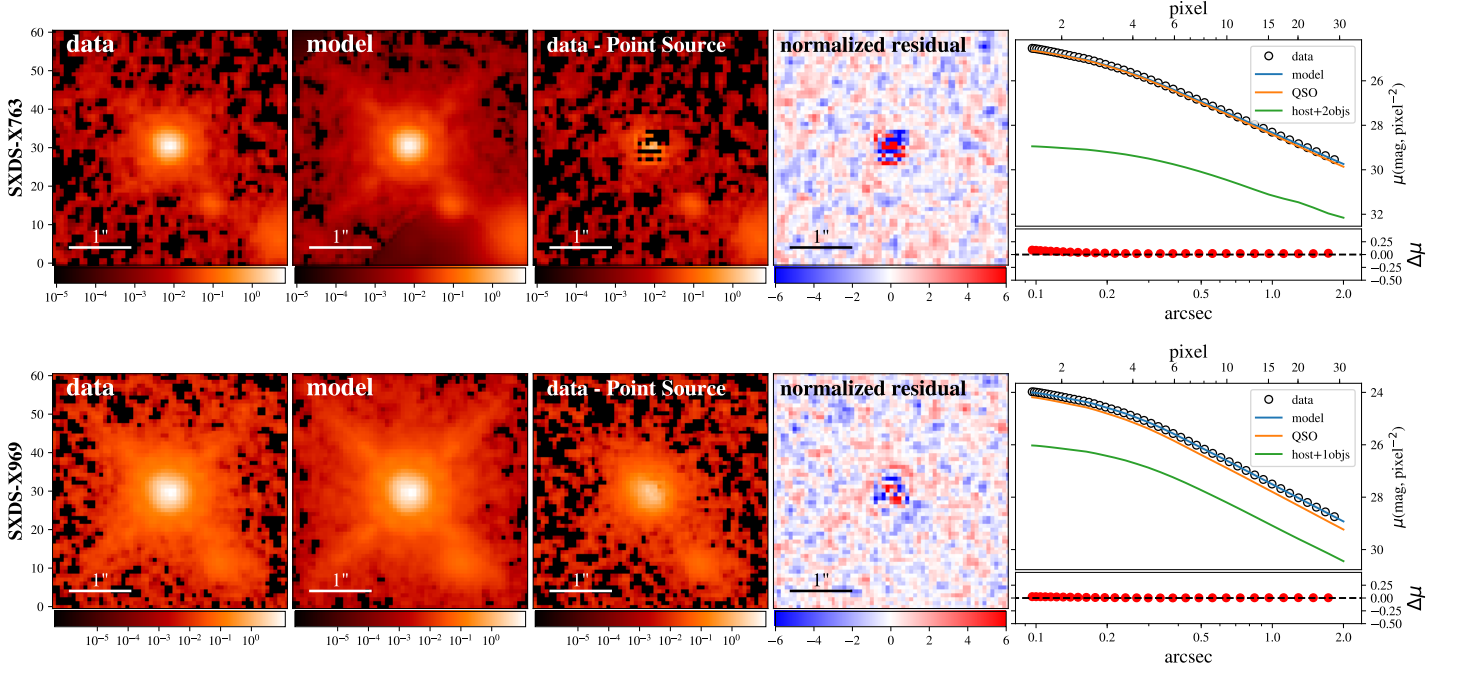


FIG. 1.— Continued.

TABLE 3
INFERRED HOST GALAXY PROPERTIES FOR THE 32 SYSTEMS.

Target ID	WFC3					ACS/F814W			host properties	
	reduced χ^2	host-total flux ratio	R_{eff} ($''$)	Sérsic n	magnitude (AB system)	reduced χ^2	host-total flux ratio	magnitude (AB system)	$\log L_R$ ($L_{\odot,R}$)	$\log M_*$ (M_{\odot})
(1)	(2)	(3)	(4)	(5)	(6)	(7)	(8)	(9)	(10)	(11)
CID1174	2.307	42% \pm 12%	0''.31 \pm 0''.07	1.9 \pm 1.3	21.48 $^{+0.37}_{-0.28}$	2.496	11% \pm 1%	23.21 $^{+0.11}_{-0.10}$	11.05 $^{+0.15}_{-0.11}$	10.78 $^{+0.18}_{-0.15}$
CID1281	1.322	49% \pm 14%	0''.24 \pm 0''.09	3.2 \pm 1.5	22.88 $^{+0.36}_{-0.27}$	1.378	19% \pm 8%	24.83 $^{+0.60}_{-0.38}$	10.41 $^{+0.15}_{-0.11}$	10.14 $^{+0.18}_{-0.15}$
CID206	2.054	35% \pm 24%	0''.29 \pm 0''.15	3.1 \pm 2.5	21.82 $^{+1.30}_{-0.58}$	1.903	8% \pm 2%	23.67 $^{+0.40}_{-0.29}$	10.86 $^{+0.52}_{-0.23}$	10.59 $^{+0.53}_{-0.25}$
CID216	1.514	94% \pm 5%	0''.25 \pm 0''.06	6.2 \pm 1.2	21.51 $^{+0.05}_{-0.05}$	1.425	35% \pm 2%	23.45 $^{+0.05}_{-0.05}$	11.05 $^{+0.03}_{-0.03}$	10.78 $^{+0.10}_{-0.10}$
CID237	2.349	30% \pm 6%	0''.87 \pm 0''.17	4.7 \pm 1.7	21.28 $^{+0.26}_{-0.21}$	2.354	3% \pm 2%	23.72 $^{+1.04}_{-0.52}$	11.18 $^{+0.11}_{-0.09}$	10.91 $^{+0.14}_{-0.13}$
CID255	1.625	19% \pm 5%	0''.19 \pm 0''.06	4.2 \pm 1.5	21.61 $^{+0.37}_{-0.28}$	2.858	4% \pm 2%	22.89 $^{+0.60}_{-0.39}$	11.08 $^{+0.15}_{-0.11}$	10.81 $^{+0.18}_{-0.15}$
CID3242	2.751	46% \pm 13%	0''.20 \pm 0''.16	6.1 \pm 1.9	21.16 $^{+0.35}_{-0.26}$	2.596	5% \pm 1%	23.60 $^{+0.34}_{-0.26}$	11.16 $^{+0.14}_{-0.11}$	10.89 $^{+0.17}_{-0.15}$
CID3570	1.665	77% \pm 2%	0''.70 \pm 0''.01	0.7 \pm 0.1	21.16 $^{+0.02}_{-0.02}$	1.332	86% \pm 2%	22.97 $^{+0.01}_{-0.01}$	10.98 $^{+0.02}_{-0.02}$	10.71 $^{+0.10}_{-0.10}$
CID452	1.684	75% \pm 4%	0''.37 \pm 0''.02	1.4 \pm 0.2	21.18 $^{+0.06}_{-0.06}$	1.452	38% \pm 1%	22.73 $^{+0.02}_{-0.02}$	11.13 $^{+0.03}_{-0.03}$	10.86 $^{+0.10}_{-0.10}$
CID454	2.203	36% \pm 3%	0''.39 \pm 0''.02	0.6 \pm 0.1	21.20 $^{+0.08}_{-0.07}$	1.291	9% \pm 1%	23.35 $^{+0.06}_{-0.06}$	11.11 $^{+0.04}_{-0.04}$	10.84 $^{+0.10}_{-0.10}$
CID50	5.576	17% \pm 9%	0''.16 \pm 0''.11	3.2 \pm 2.2	20.93 $^{+0.86}_{-0.48}$	4.940	5% \pm 3%	22.50 $^{+1.15}_{-0.55}$	11.07 $^{+0.35}_{-0.19}$	10.80 $^{+0.36}_{-0.21}$
CID543	1.902	31% \pm 10%	0''.10 \pm 0''.00	0.5 \pm 0.3	21.99 $^{+0.41}_{-0.30}$	1.435	5% \pm 2%	23.77 $^{+0.53}_{-0.36}$	10.70 $^{+0.16}_{-0.12}$	10.43 $^{+0.19}_{-0.15}$
CID597	1.565	42% \pm 17%	0''.17 \pm 0''.06	1.8 \pm 0.8	21.87 $^{+0.54}_{-0.36}$	1.254	12% \pm 1%	23.56 $^{+0.13}_{-0.11}$	10.73 $^{+0.22}_{-0.15}$	10.46 $^{+0.24}_{-0.18}$
CID607	1.692	44% \pm 18%	0''.21 \pm 0''.09	3.4 \pm 1.1	21.19 $^{+0.58}_{-0.37}$	2.590	5% \pm 2%	23.57 $^{+0.51}_{-0.35}$	11.02 $^{+0.23}_{-0.15}$	10.75 $^{+0.25}_{-0.18}$
CID70	2.041	20% \pm 5%	0''.42 \pm 0''.10	3.6 \pm 1.0	21.86 $^{+0.30}_{-0.24}$	2.361	2% \pm 1%	24.63 $^{+0.68}_{-0.41}$	10.98 $^{+0.12}_{-0.10}$	10.72 $^{+0.16}_{-0.14}$
LID1273	1.697	53% \pm 9%	0''.30 \pm 0''.04	1.2 \pm 0.5	20.94 $^{+0.21}_{-0.18}$	2.137	6% \pm 1%	23.29 $^{+0.15}_{-0.15}$	11.32 $^{+0.09}_{-0.07}$	11.05 $^{+0.13}_{-0.12}$
LID1538	2.362	44% \pm 8%	0''.18 \pm 0''.04	2.8 \pm 0.5	21.25 $^{+0.22}_{-0.18}$	2.173	8% \pm 1%	23.09 $^{+0.19}_{-0.16}$	11.12 $^{+0.09}_{-0.08}$	10.86 $^{+0.13}_{-0.12}$
LID360	3.918	18% \pm 2%	0''.63 \pm 0''.02	0.8 \pm 0.4	21.46 $^{+0.14}_{-0.12}$	4.914	4% \pm 1%	23.25 $^{+0.17}_{-0.15}$	11.08 $^{+0.06}_{-0.05}$	10.81 $^{+0.11}_{-0.11}$
XID2138	1.597	39% \pm 6%	0''.50 \pm 0''.03	1.2 \pm 0.4	21.87 $^{+0.17}_{-0.15}$	2.731	5% \pm 1%	23.90 $^{+0.31}_{-0.24}$	10.89 $^{+0.07}_{-0.06}$	10.63 $^{+0.12}_{-0.12}$
XID2202	3.23	33% \pm 8%	0''.10 \pm 0''.00	4.0 \pm 1.0	21.16 $^{+0.30}_{-0.24}$	3.852	8% \pm 2%	22.59 $^{+0.29}_{-0.23}$	11.15 $^{+0.12}_{-0.10}$	10.88 $^{+0.16}_{-0.14}$
XID2396	3.669	24% \pm 11%	0''.58 \pm 0''.09	0.8 \pm 1.4	21.40 $^{+0.65}_{-0.40}$	5.346	2% \pm 1%	23.36 $^{+0.24}_{-0.20}$	11.12 $^{+0.26}_{-0.16}$	10.85 $^{+0.28}_{-0.19}$
CDFS-1	1.358	65% \pm 20%	0''.14 \pm 0''.07	4.8 \pm 1.1	22.47 $^{+0.40}_{-0.29}$	10.71 $^{+0.16}_{-0.12}$	10.45 $^{+0.19}_{-0.15}$
CDFS-229	4.329	18% \pm 2%	0''.51 \pm 0''.03	0.5 \pm 0.2	21.57 $^{+0.14}_{-0.13}$	10.90 $^{+0.06}_{-0.05}$	10.63 $^{+0.12}_{-0.11}$
CDFS-321	3.998	25% \pm 12%	0''.38 \pm 0''.12	2.3 \pm 2.0	20.34 $^{+0.70}_{-0.42}$	11.52 $^{+0.28}_{-0.17}$	11.25 $^{+0.30}_{-0.20}$
CDFS-724	1.355	35% \pm 15%	0''.12 \pm 0''.03	1.6 \pm 1.1	23.70 $^{+0.58}_{-0.38}$	10.06 $^{+0.23}_{-0.15}$	9.79 $^{+0.25}_{-0.18}$
ECDFS-358	2.012	56% \pm 14%	0''.36 \pm 0''.04	1.7 \pm 0.5	21.34 $^{+0.30}_{-0.24}$	11.16 $^{+0.12}_{-0.10}$	10.89 $^{+0.16}_{-0.14}$
SXDS-X1136	1.937	41% \pm 8%	0''.10 \pm 0''.00	2.0 \pm 0.5	21.92 $^{+0.23}_{-0.19}$	10.75 $^{+0.09}_{-0.08}$	10.49 $^{+0.14}_{-0.13}$
SXDS-X50	1.423	41% \pm 9%	0''.19 \pm 0''.04	1.7 \pm 0.6	21.99 $^{+0.27}_{-0.21}$	10.80 $^{+0.11}_{-0.09}$	10.54 $^{+0.15}_{-0.13}$
SXDS-X717	1.426	61% \pm 9%	0''.26 \pm 0''.07	5.6 \pm 1.4	21.76 $^{+0.18}_{-0.15}$	10.77 $^{+0.07}_{-0.06}$	10.51 $^{+0.12}_{-0.12}$
SXDS-X735	2.203	32% \pm 9%	0''.22 \pm 0''.06	2.0 \pm 1.0	20.92 $^{+0.33}_{-0.25}$	11.19 $^{+0.13}_{-0.10}$	10.92 $^{+0.17}_{-0.14}$
SXDS-X763	2.376	6% \pm 4%	0''.69 \pm 0''.53	2.4 \pm 0.8	24.13 $^{+1.17}_{-0.55}$	9.95 $^{+0.47}_{-0.22}$	9.68 $^{+0.48}_{-0.24}$
SXDS-X969	1.613	29% \pm 11%	0''.11 \pm 0''.02	2.1 \pm 1.1	21.59 $^{+0.52}_{-0.35}$	11.03 $^{+0.21}_{-0.14}$	10.76 $^{+0.23}_{-0.17}$

NOTE. — Column 1: Object ID. Column 2-6: WFC3 inference. Column 2: Reduced χ^2 value by the best PSF in the library. Column 7-9: ACS inference. Column 10: Observed host luminosity in the rest-frame R band. Column 11: Host total stellar mass.

TABLE 4
INFERRED \mathcal{M}_{BH} .

Target ID (1)	using emission line $H\alpha$				using emission line $H\beta$			
	FWHM (km s^{-1}) (2)	$\log(\lambda L_{H\alpha})$ (erg s^{-1}) (3)	\mathcal{M}_{BH} (M_{\odot}) (4)	Eddington ratio ($\log \lambda$) (5)	FWHM(5100) (km s^{-1}) (6)	$\log(\lambda L_{\lambda 5100})$ (erg s^{-1}) (7)	\mathcal{M}_{BH} (M_{\odot}) (8)	Eddington ratio ($\log \lambda$) (9)
CID1174	1906	43.43	7.99	-0.50	5898	44.76	8.83	-1.35
CID1281	1619	43.24	7.75	-0.45
CID206	3334	43.48	8.53	-1.00
CID216	2230	42.85	7.85	-0.93
CID237	2112	43.86	8.29	-0.40
CID255	1932	43.99	8.27	-0.25	3709	45.37	8.73	-0.63
CID3242	2543	43.83	8.45	-0.58	3775	45.10	8.61	-0.78
CID3570	1959	43.16	7.89	-0.66
CID452	3458	42.92	8.30	-1.30	3127	44.63	8.22	-0.88
CID454	2824	43.34	8.31	-0.91
CID50	2340	43.94	8.42	-0.45	1939	45.33	8.15	-0.09
CID543	2189	43.57	8.19	-0.56
CID597	1656	43.33	7.81	-0.42
CID607	3009	43.67	8.53	-0.81	4242	44.78	8.56	-1.06
CID70	2480	43.51	8.27	-0.71	3982	45.16	8.69	-0.80
LID1273	3224	43.61	8.56	-0.90
LID1538	2941	43.60	8.47	-0.83
LID360	2482	43.88	8.45	-0.53	2869	45.09	8.37	-0.55
XID2138	3186	43.61	8.55	-0.89	2945	44.81	8.25	-0.72
XID2202	2973	43.56	8.46	-0.85
XID2396	2271	44.06	8.46	-0.37	2658	45.50	8.51	-0.27
CDFS-1	5449	43.08	8.79	-0.98
CDFS-229	2254	43.30	8.08	-0.48
CDFS-321	2442	43.93	8.46	-0.50
CDFS-724	3352	42.56	8.09	-1.22
ECDFS-358	2237	43.40	8.12	-0.67
SXDS-X1136	2760	43.43	8.33	-0.85	6761	44.71	8.93	-1.50
SXDS-X50	1817	43.42	7.94	-0.47
SXDS-X717	2931	43.05	8.20	-1.08
SXDS-X735	2702	43.70	8.44	-0.70	3520	45.07	8.54	-0.73
SXDS-X763	2961	43.57	8.47	-0.84	4509	44.51	8.47	-1.27
SXDS-X969	2296	43.50	8.20	-0.64	1696	45.05	7.90	-0.11

NOTE. — Column 1: Object ID. Column 2-4: $H\alpha$ emission line width (FWHM), continuum luminosity, and inferred \mathcal{M}_{BH} . Column 5-7: $H\beta$ emission line width (FWHM), continuum luminosity, and inferred \mathcal{M}_{BH} .

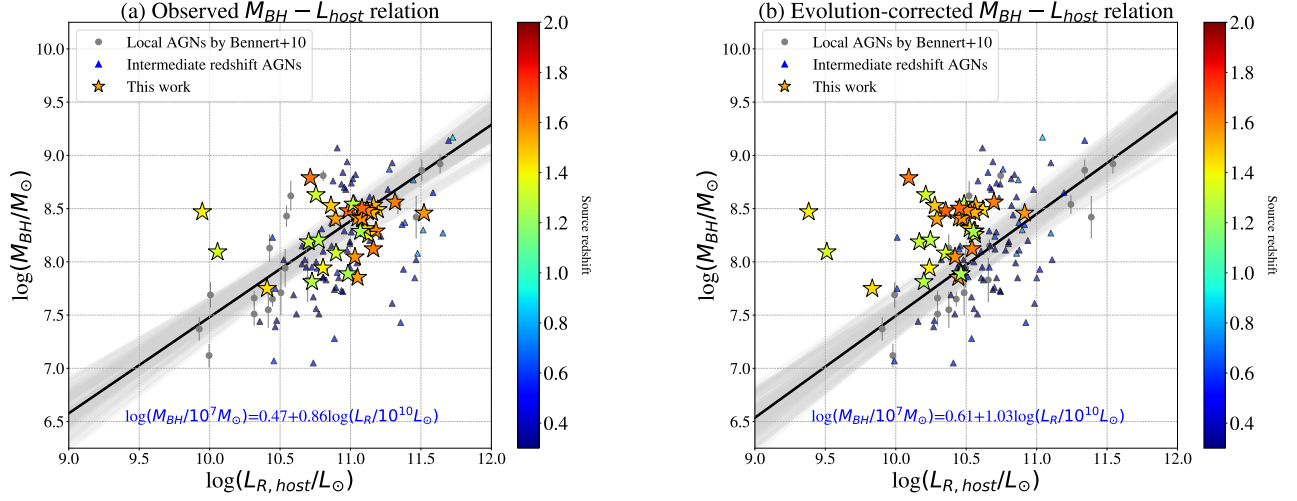


FIG. 4.— Illustration of observed (left) and evolution-corrected (right) correlations between \mathcal{M}_{BH} - L_{host} , with local linear relation indicated. The redshift are color-coded, for distant and intermediate AGNs.

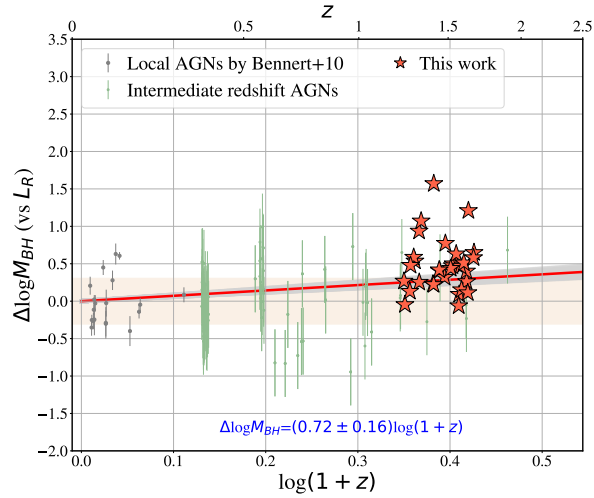


FIG. 5.— Illustration of the offset in $\log \mathcal{M}_{\text{BH}}$ (vs. L_R) as a function of redshift. The orange band is the intrinsic scatter of local linear relation.

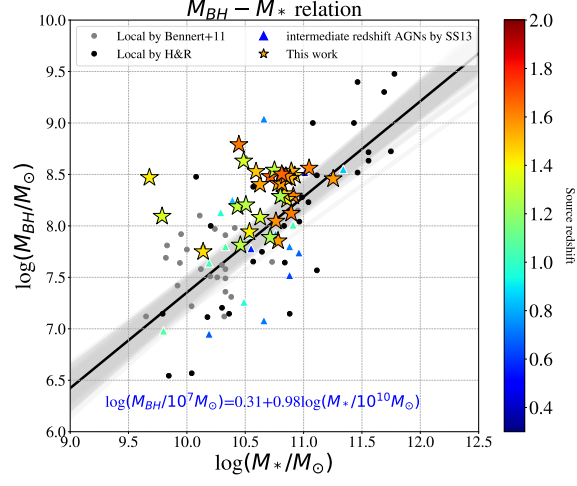


FIG. 6.— Similar to the Figure 4, but the comparison of the $\mathcal{M}_{\text{BH}}-M_*$ relations.

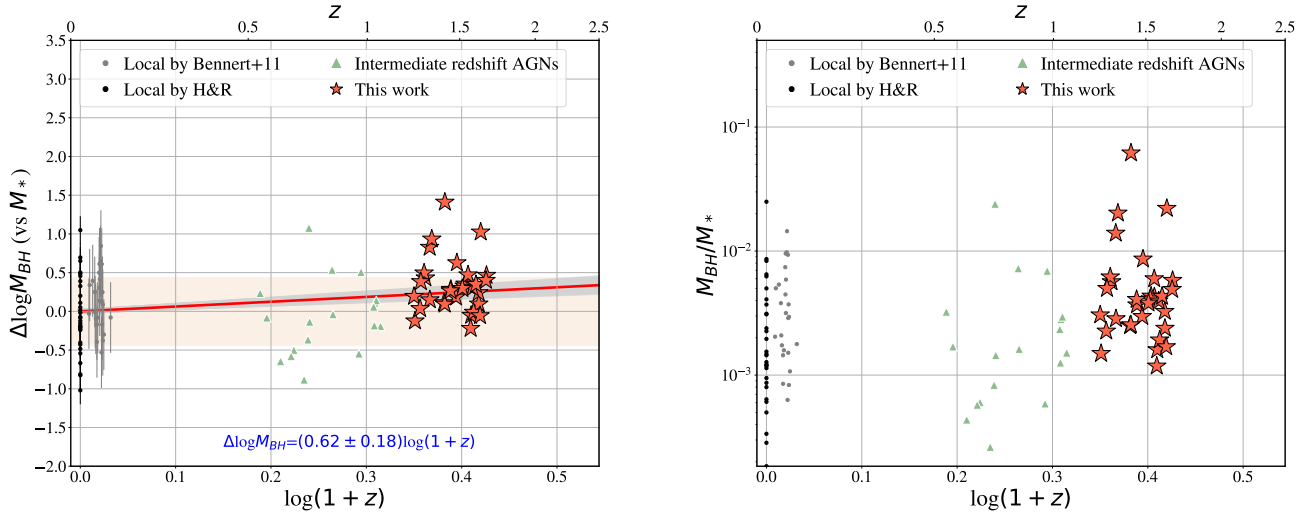


FIG. 7.— Left: illustration of the offset in $\log \mathcal{M}_{\text{BH}}$ (vs. M_*) as a function of redshift. Right: redshift evolution of the $\mathcal{M}_{\text{BH}}/M_*$.

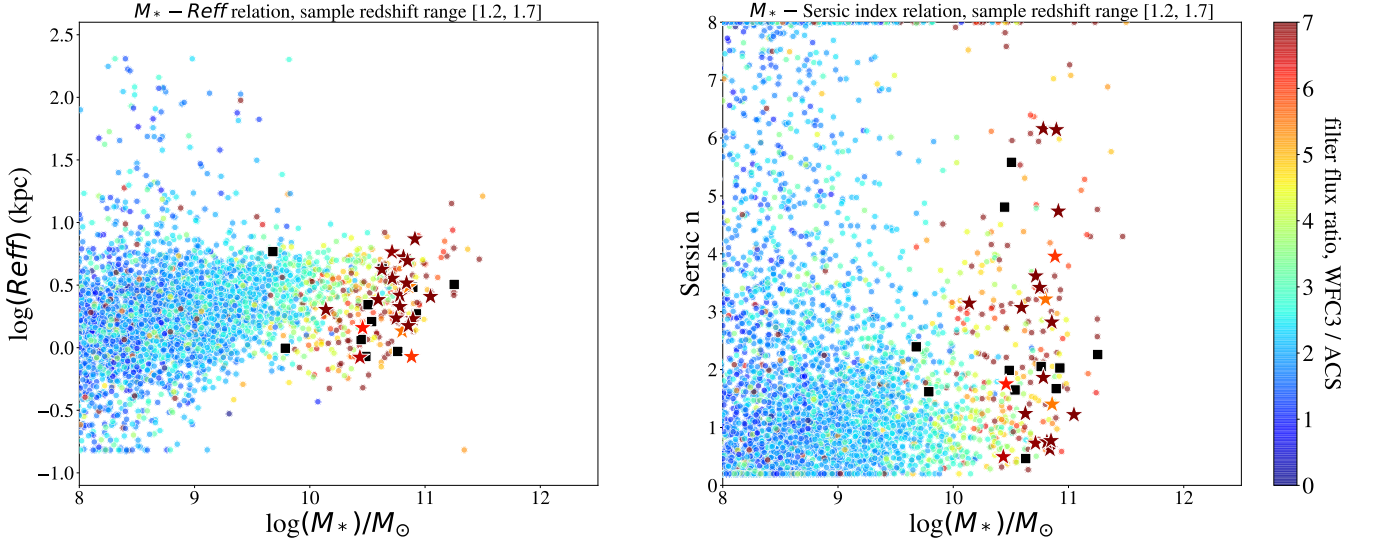


FIG. 8.— The comparison of the galaxy properties between our 32 AGNs' hosts to the 4401 CANDLE inactive sample (circles). The color coding is based on the filter flux ratio between WFC3 and ACS. For CANDLE sample, the WFC3/F125W flux is taken. The black squares are the AGN samples with only WFC3 band observation.

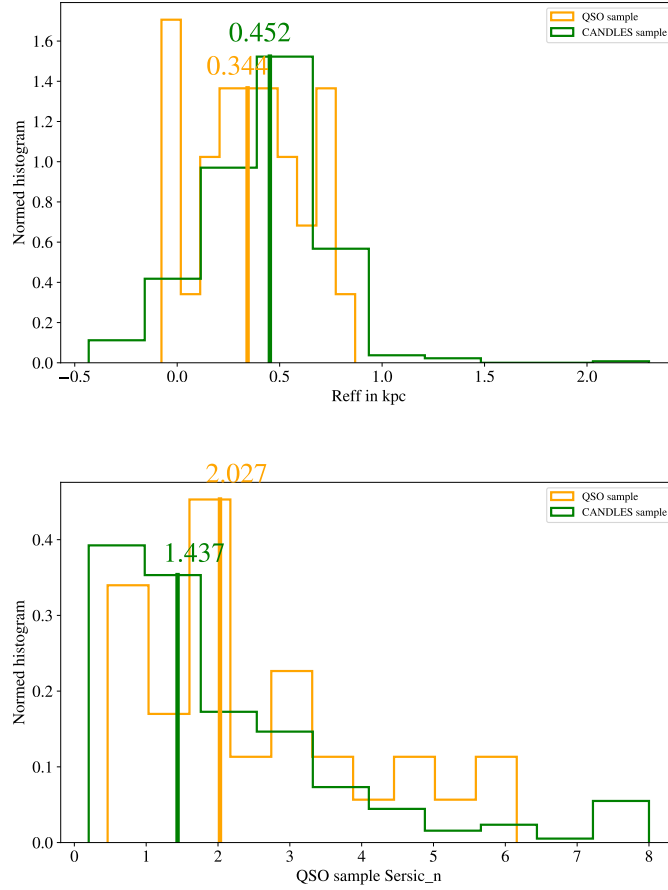


FIG. 9.— The comparison of the histogram of the $Reff$ and Sérsic n , with median value indicated.